

Accurate large-scale simulations of siliceous zeolites by neural network potentials

Andreas Erlebach¹, Petr Nachtigall¹, & Lukáš Grajciar^{1*}

¹*Department of Physical and Macromolecular Chemistry, Charles University, Hlavova 8, 128 43 Praha 2*

The computational discovery and design of zeolites is a crucial part of the chemical industry. Finding highly accurate while computationally feasible protocol for identification of hypothetical zeolites that could be targeted experimentally is a great challenge. To tackle the challenge, we trained neural network potentials (NNP) with the SchNet architecture on a structurally diverse database of density functional theory (DFT) data. This database was iteratively extended by active learning to cover not only low-energy equilibrium configurations but also high-energy transition states. We demonstrate that the resulting reactive NNPs retain the accuracy of the DFT reference for thermodynamic stabilities, vibrational properties, and reactive and non-reactive phase transformations. The novel NNPs outperforms specialized, analytical force fields for silica, such as ReaxFF, by order(s) of magnitude in accuracy, while speeding up the calculations in comparison to DFT by at least three orders of magnitude. As a showcase, we screened an existing zeolite database containing 330 thousand structures and revealed more than 20 thousand additional hypothetical frameworks in the thermodynamically accessible range of zeolite synthesis. Hence, our NNPs are expected to be essential for future high-throughput studies on the structure and reactivity of hypothetical and existing zeolites.

Keywords: zeolite databases, machine learning, neural networks, reactive force fields, phase transitions

*E-mail: lukas.grajciar@natur.cuni.cz

1. Introduction

Zeolites are of central importance for numerous industrial applications ranging from catalysis through adsorption to ion exchange,¹ owing to their highly diverse structures and properties. Theoretically, there are more than two million^{2–5} possible zeolite frameworks but only 240 zeolite frameworks listed in the IZA database^{6,7} have been prepared so far, a discrepancy known as the zeolite conundrum.⁵ Therefore, ongoing research focuses on sophisticated synthesis routes, like the ADOR protocol,⁸ allowing the preparation of novel, unfeasible zeolites that are not accessible by standard solvothermal procedures.^{9–11} Another way to prepare new feasible or unfeasible zeolites is the polymorphous inter-zeolite transformation under elevated temperature or pressure.^{12–16} Finding reliable and computational feasible protocol for identification of hypothetical zeolites that could be synthesized experimentally is still a great challenge.

In order to guide the ongoing search for new zeolites, computer simulations proved indispensable yet challenging for the (pre-)screening of structures and properties. Such a screening performed by Deem et al. allowed to narrow down the number of possible zeolite frameworks to thermodynamically accessible ones.^{3,4} This Deem database generated by atomistic simulations using analytical force fields contains about 330 thousand hypothetical zeolites. Other computational studies used the IZA and Deem databases to estimate the feasibility of hypothetical zeolites and formulated design rules for their targeted solvothermal synthesis.^{17–20} Central quantity determining the feasibility of zeolites is the correlation between the zeolite density and energy, firstly calculated using atomistic simulations²¹ and then confirmed by experiments.²²

Recently, the advent of machine learning in materials science and chemistry enabled the search for more complex correlations of the zeolite structure, stability, and properties.²³ For example, graph similarity analysis of the Deem and IZA databases predicted thousands of possible diffusionless transformations from known to hypothetical zeolite frameworks.²⁴ Apart from zeolite synthesis,

machine learning studies also used the zeolite databases to find structure-property correlations, e.g., for mechanical properties²⁵ and gas adsorption capacities to enable the targeted zeolite synthesis.²⁶ However, the critical prerequisite for finding reliable correlations guiding experimental studies is generating accurate structural and energetic data at the atomistic level.

The atomistic simulations indeed provide vital insights into the structure and properties of zeolites.²⁷ However, realistic modeling of zeolites with *ab initio* quality is frequently hampered by the prohibitive costs of first-principles methods. For example, only a few studies used atomistic simulations investigating the collapse of zeolites under high temperatures or pressures.^{28,29} Under high temperatures and low to moderate pressures, zeolites show a two-stage transformation, first to a low-density and subsequently to a high-density amorphous phase.^{29–32} Computational studies of such phase transition used either *ab initio* simulations employing simple structure models with few atoms and short timescales²⁸ or more realistic structure models and longer timescales but with analytical (reactive) force fields.²⁹ Large-scale simulations with *ab initio* quality are therefore of fundamental importance for discovering new zeolites not only by the screening of databases but also through the understanding of reaction pathways of zeolite phase transformations.

Enabling such simulations at a large-scale requires approximate modeling of the potential energy surface (PES) that retains the accuracy of high-level quantum mechanical calculations. In recent years, numerous machine learning potentials (MLP) have been proposed that accurately interpolate the PES providing the necessary speed-up compared to *ab initio* simulations.^{33–37} Among them are neural network potentials (NNP)³³ of different types and architectures, e.g., hierarchical interacting particle NNP (HIP-NN),³⁸ tensor field networks,³⁹ and the graph convolutional NNP SchNet.^{40,41} The latter is a message-passing type NNP architecture using trainable input representations of atomic environments repeatedly refined by convolutional operations in several iterations to model many-body interactions. Tests on benchmark datasets^{35,40,41} focusing on molecular systems proved the excellent accuracy of SchNet NNPs to model energy and forces. However, little is known about

transferability and accuracy of SchNet - and message-passing type NNPs in general - for materials science related questions,³⁴ such as diffusion,⁴² phase stability⁴³ and transitions,⁴⁴ or phonon properties.⁴⁵ So far, only a few studies trained MLP for PES modeling silica using only a small number of polymorphs, surface models, amorphous and liquid configurations with limited model complexity.^{46,47} However, no MLPs considered the reactive PES of silica, including the tremendous structural diversity of zeolites.

The central aim of this work is the training of reactive SchNet NNPs for accurate and general PES modeling of silica, including the structural diversity of zeolites over a wide density range. Training of an NNP ensemble allows active learning for iterative extension of the reference dataset and refinement of the NNP.^{33,48} The final dataset covers the silica configuration space ranging from low-density zeolites to high-pressure polymorphs, including low-energy equilibrium structures and high-energy transition states. This allows interpolation of the PES for accurate and transferable modeling of siliceous zeolites within the most relevant parts of the configuration space and enables the required large-scale simulations with *ab initio* accuracy.

The novel NNPs facilitated the reoptimization of the Deem database with unprecedented accuracy providing vital input for future machine learning studies to find correlations between structure, stability, and properties of zeolites. The database reoptimization also revealed more than 20k new hypothetical zeolites in the thermodynamically accessible range of zeolite synthesis. In addition, rigorous accuracy tests of the NNPs showed excellent agreement with DFT and experimental results, including not only equilibrium structures and phonon properties but also silica phase transformations under extreme conditions such as glass melting and the thermal collapse of zeolites. The trained NNPs show an accuracy improvement of about one order of magnitude for modeling energy and forces compared to other PES approximations: two state-of-the-art analytical force fields including the non-reactive Sanders-Leslie-Catlow (SLC) potential^{49,50} and the reactive silica force field ReaxFF of Fogarty et al.,⁵¹ and one tight-binding DFT parameterization GFN0-

xTB.⁵² Consequently, this work provides a computational tool for accurate, reactive modeling of siliceous zeolites for their targeted design and synthesis.

2. Results

Key prerequisite for the training of NNPs is the generation of a diverse dataset covering the variety of atomic structures and densities of zeolites in both low and high-energy parts of the PES to accurately model structure, equilibrium properties, and phase transitions. The description of the NNPs training and dataset details are provided in Section 4. When confronting NNPs results with the available experimental results it must be stressed that NNPs cannot outperform the reference level of theory. However, accurate NNPs helps us to understand the accuracy of the reference level of theory with respect to experiment providing that trained NNPs retains the accuracy of the reference level of theory. Highly accurate NNPs can be used for the simulations of experimental observable using more realistic models and longer simulation times than possibly allowed with the reference level of theory. Thus, the accuracy of the trained NNPs is demonstrated first (Section 2.1) while the performance with respect to experimental data is described in following subsections (2.2-2.4).

2.1 Accuracy compared to other methods

The NNP accuracy, together with the accuracy of the commonly used SLC potential, a reactive force field (ReaxFF), and one tight-binding DFT implementation (GFN0-xTB), is evaluated for the set of single-point energy calculations on a test set of structures taken from the NNPs can simulations (Sections 2.2-2.4). This test set contains 1460 configurations including (i) close to equilibrium (EQ) structures from the NNPs can optimized zeolite databases (see Section 2.2), (ii) silica bilayer configurations of the Stone-Wales defect formation (see Section 2.4), and (iii) high-energy structures from the glass melting and zeolite amorphization (ZA) simulations (see Section 2.4). These structures were not included in the reference dataset for NNP training. The entire test

set can be found in the Zenodo repository (<https://doi.org/10.5281/zenodo.5827897>).

Table 1: Root mean square (RMSE) and mean absolute error (MAE) of energies [meV/atom] and forces [eV/Å] calculated for all test cases and only for equilibrium configurations (EQ) with respect to SCAN+D3 results. NNP results include calculations of a single potential (sNNP) and an ensemble of six NNPs (eNNP).

Level of theory	Energy (EQ)		Forces (EQ)		Energy (all)		Forces (all)	
	MAE	RMSE	MAE	RMSE	MAE	RMSE	MAE	RMSE
sNNPscan	2.99	4.20	0.048	0.070	3.90	5.44	0.175	0.303
eNNPscan	2.83	3.95	0.046	0.067	3.83	5.49	0.155	0.265
SLC	88.0	111	2.612	3.431	207	313	3.206	4.166
ReaxFF	56.4	78.4	1.266	2.996	88.8	136	2.789	8.533
GFN0-xTB	57.5	106	0.302	0.787	127	201	0.735	3.391

Table 1 summarizes the MAE and RMSE of energies and forces of all methods with respect to SCAN+D3 results (supplementary Table S1 shows PBE+D3 results). Figure 1 shows the corresponding energy error distributions. In addition, supplementary Table S2 lists the errors for a test set that includes the configurations of the extrapolated part of the ZA simulations. In the case of EQ structures, NNPscan energies are in best agreement with SCAN+D3 calculations with an RMSE of less than 4.2 and 3.95 meV/atom. The analytical potentials (SLC, ReaxFF) and GFN0-xTB show higher errors by more than one order of magnitude. Such energy errors (\sim 100 meV/atom) translate into uncertainties of zeolite phase stability calculations as described in Section 2.2 (cf. Figure 2) of about 30 kJ/(mol Si). The fairly good agreement of SLC with experimental and DFT results (cf. supplementary Table S3) applies only to existing, siliceous zeolites but not to the rigorous test set that includes existing non-siliceous and hypothetical frameworks. Therefore, the novel NNPs provide a sufficiently accurate PES covering much larger configurational space than SLC allowing reliable prediction of zeolite topologies that could be thermodynamically accessible, e.g., via

alternative synthesis routes beyond solvothermal methods.

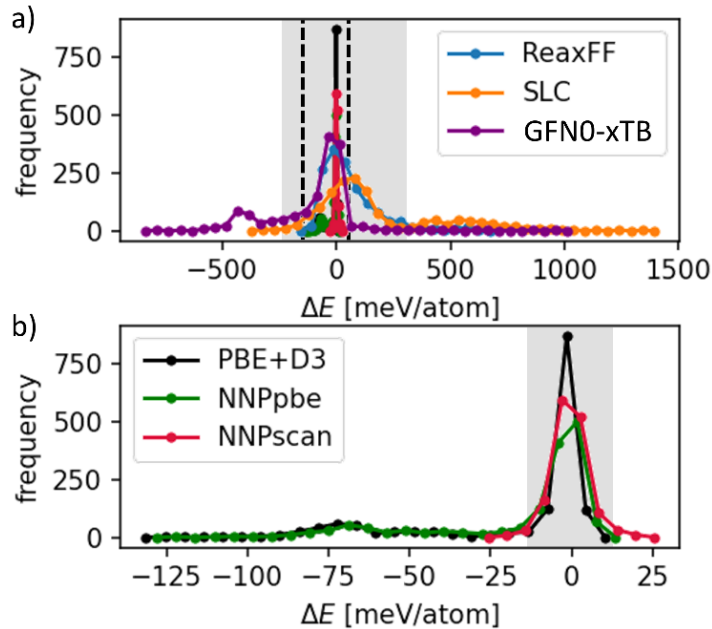


Figure 1: Error distribution of energies ΔE with respect to SCAN+D3 of (a) analytical force fields (SLC, ReaxFF) and tight binding DFT (GFN0-xTB) as well as PBE+D3 and the new NNPs (NNPpbe, NNPscan). Error distribution of frequencies with respect to SCAN+D3 is shown in part (b) for new NNPs. Dashed lines in (a) show the energy range of (b), and shaded areas indicate the approximate range of energy errors for equilibrium structures (EQ, *cf.* Table 1).

It must be stressed that the trained NNPs approximate energies and forces of the reference level DFT with high accuracy even for high energy structures and transition states (Table 1). For example, the glass melting simulations at high temperatures yielded energy differences between PBE+D3 and SCAN+D3 of more than 50 meV/atom (Fig. 1b). In contrast, the NNPscan energies deviate about 10-25 meV/atom from their DFT reference for the same glass melting trajectories. In addition, even the errors of the extrapolated configurations of the ZA simulations (up to 40 meV/atom) are at least three times lower than the RMSEs of SLC, ReaxFF, and GFN0-xTB. Among the latter, ReaxFF

tailored for the elements Si, O, and H⁵¹ provides the lowest energy errors but with an RMSE of 136 meV/atom. Recently, a benchmark study of ReaxFF potentials (parameterized for C, O, H) reported similar energy RMSEs of about 100 meV/atom for hydrogen combustion reactions.⁵³ On the other hand, GFN0-xTB allows a more general modeling with a parameterization for 86 elements focusing on equilibrium structures and frequency calculations.⁵² Therefore, GFN0-xTB shows a larger energy RMSE for transition state structures (*cf.* Fig. 1a) yet gives higher force accuracy than the silica potentials SLC and ReaxFF. Finally, using an ensemble of six tailor-made silica NNPs provides only a little improvement over single NNP calculations, the latter achieves the best performance in terms of accuracy and computational effort for the reactive modeling of silica.

2.2 Zeolite databases

The new NNPs enable the reoptimization of the Deem and IZA database (available at: <https://doi.org/10.5281/zenodo.5827897>) to provide highly accurate input for investigations of structure-property relationships of existing and hypothetical zeolites. Figure 2 compares the relative energies and framework densities of the NNPscan optimized databases with the results from the SLC analytical potential, a state-of-the-art analytical potential for silicious zeolites, taken from Ref. 3 (www.hypotheticalzeolites.net, accessed: November 29, 2019). Only the low-density zeolite analogue RWY⁵⁴ (Ga₂GeS₆) is not shown in Fig. 2 (NNPscan: 61 kJ/mol, 7.86 Si/nm³; SLC: 104.2 kJ/mol, 7.62 Si/nm³).

Energies and densities of the SLC optimizations show a clear qualitative correlation with NNPscan results (Fig. 2b). The Pearson correlation coefficients are 0.89 and 0.98 for energies and densities, respectively. However, the SLC results show systematically higher relative energies than NNPscan for zeolites at high energies and densities, probably due to the energetic overestimation of structural features in those zeolites. For example, SLC yielded up to 20 kJ/(mol Si) higher energies for three-ring containing zeolites such as OBW, OSO, NAB, and JOZ that can only be synthesized if Be is

incorporated in the framework (see supplementary Fig. S1).⁵⁵

To verify that NNPscan shows improved accuracy compared to SLC, supplementary Table S3 compares the NNP and SLC results with experimentally available relative enthalpies and densities of 15 siliceous zeolites and five silica polymorphs.^{6,7,56} Additionally, DFT optimizations were applied to a subset of five zeolites and five polymorphs. Figure 2c shows the corresponding energy-density plot of the selected zeolites.

The analytical SLC potential shows relatively good agreement with experimental results in the case of purely siliceous zeolites along with a 4.0 kJ/(mol Si) mean absolute error (MAE) in energies. However, SLC systematically overestimates the experimentally observed enthalpies (see Fig. 2c and supplementary Table S3). In contrast, the trained NNPscan achieved a substantial accuracy improvement with an energy MAE of 2.2 kJ/(mol Si). Structure optimizations at the SCAN+D3 level of a smaller subset give MAE similar to the NNPscan, namely, 2.7 kJ/(mol Si). The MAEs of atomic densities show a similar trend as that for relative energies, that is, the NNPs provide significantly higher quality than SLC for quantitative structural and energetic predictions of siliceous zeolites.

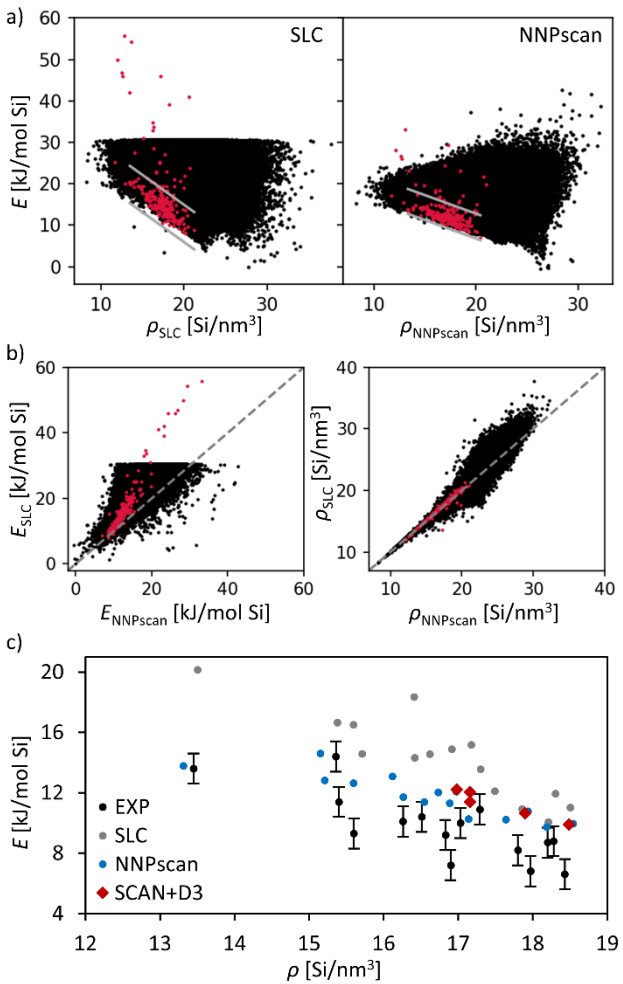


Figure 2: Relative energies E with respect to α -quartz as a function of framework density ρ (a) of hypothetical (black) and existing (red) zeolite frameworks calculated using SLC and NNPscan. Solid lines in (a) indicate the energy-density range of purely siliceous zeolites (cf. supplementary Fig. S1). (b) Correlations of energies and densities obtained at the NNPscan and SLC level. (c) Comparison of simulation results with experimental (EXP) values (cf. supplementary Table S3). Error bars correspond to an estimated experimental accuracy of ± 1 kJ/(mol Si).⁵⁶

Therefore, reoptimization of the Deem database using NNPscan provides significantly improved input for the computational design and discovery of new zeolite frameworks by analyzing structure, energy, and density correlations for hypothetical and existing frameworks.^{3,4,17–20} The solid lines in Fig. 2a show the range of relative energies and densities of the 40 zeolite frameworks that have

been successfully synthesized in their purely siliceous form (*cf.* supplementary Fig. S1).⁵⁷ The SLC calculated (relative) energies and densities range from approximately 4-24 kJ/(mol Si) and 13.5-21.2 Si/nm³, respectively. On the other hand, NNPscan optimizations yield a narrower energy range of 6-19 kJ/(mol Si) but similar densities of 13.3-20.4 Si/nm³ (dashed lines in Figure S1). Hypothetical zeolites within these energy ranges can be considered as thermodynamically accessible by solvothermal synthesis methods. In the case of SLC, this applies to 32794 frameworks of the Deem database. However, due to the systematically overestimated SLC energies, more than 20 thousand additional hypothetical zeolites (total of 53134) were obtained from NNPscan calculations that fulfill the stability criterion mentioned above (*cf.* Fig. S2). These results demonstrate the crucial importance of accurate large-scale simulations of equilibrium structures for the discovery of zeolites.

2.3 Vibrational properties

In addition to simulations of equilibrium configurations at zero Kelvin, calculations of vibrational properties or free energies at elevated temperatures require accurate modeling of close to equilibrium structures and forces on atoms. To test the reliability of SCAN+D3 and NNPscan for predicting the vibrational density of states (VDOS), the VDOS of α -cristobalite was calculated at both levels. Figure 3a shows both VDOS along with the experimentally observed one.⁵⁸ Since α -cristobalite was part of the reference database, we performed additional VDOS calculations (NNPscan level) on virtuous silica structures not considered in the NNP training procedure. Three amorphous silica structures were generated using independent simulated annealing MD runs (*cf.* Method section). The obtained VDOS for the glass models are virtually identical (*cf.* supplementary Fig. S3), demonstrating sufficient sampling of amorphous structures. Figure 3b shows the average of the three calculated VDOS along with experimental results^{59,60} and DFT simulations⁶¹ at the LDA level (Perdew-Zunger exchange-correlation functional). Please note, the VDOS calculations at the DFT level employed the finite-difference approach (FD) using the harmonic approximation while the NNPscan level calculations used MD simulations at 300 K for calculation of the velocity-

autocorrelation function (VACF, *cf.* Method section). The latter approach includes anharmonic effects, *i.e.*, the temperature-dependent shift of vibrational frequencies. However, at low temperatures such as 300 K, only minor frequency shifts in the order of 0.1 THz are expected (e.g., as shown before for Al_2O_3 ,⁶² MgSiO_3 ⁶³) not influencing the comparison of different PES approximations shown in Figure 3.

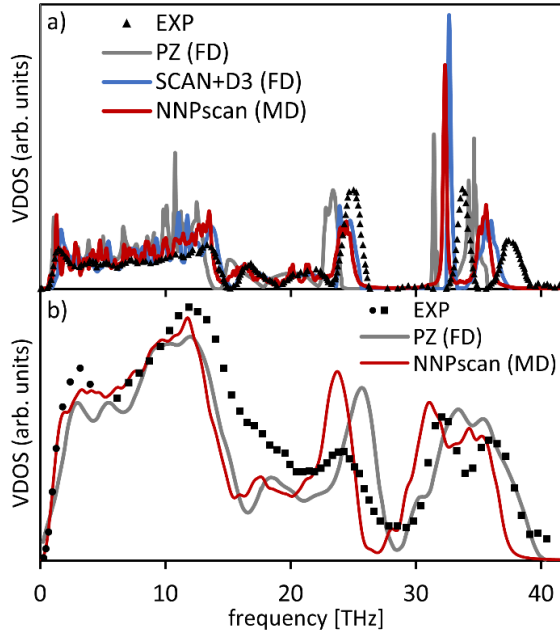


Figure 3: Vibrational density of states (VDOS) of (a) α -cristobalite and (b) silica glass obtained from experiments (black triangles: Ref. 58, dots: Ref. 59, squares: Ref. 60), DFT (LDA functional PZ: taken from Refs. 58 and 61, SCAN+D3: this work) and NNPscan calculations. VDOS were calculated using the velocity-autocorrelation from MD simulations (at 300 K) or the finite-difference (FD) approach.

In the case of α -cristobalite, the VDOS calculated at the NNPscan and SCAN+D3 level are almost identical with maximum frequency deviations of about 0.4 THz. Up to frequencies of ca. 25 THz, the calculated VDOS show excellent agreement with experiments. However, both SCAN+D3 and NNPscan underestimate the two highest frequency modes by up to 2 THz showcasing that the

trained NNPs retain DFT accuracy. Even higher deviations from experiment of up to 3 THz are observed for the VDOS calculated using the PZ functional. We obtained similar errors at the NNPscan level when the FD approach was applied to calculate the harmonic VDOS (see supplementary Fig. S4) leading to frequency differences between NNPscan and SCAN+D3 of up to 1.5 THz. Such frequency changes are not connected with anharmonic (temperature) effects as described above.^{62,63} Most likely, the FD approach is prone to minor force errors of the few single-point calculations required to compute the VDOS. In contrast, the employed MD approach samples the VACF over a trajectory with several thousand microstates, probably facilitating a certain cancellation of the force errors and resulting in a better agreement with the SCAN+D3 FD results.

Since the MD approach proved more accurate for VDOS calculations at the NNPscan level, this procedure was also applied to the VDOS calculations of vitreous silica. Similar to α -cristobalite, the NNPscan calculated VDOS agrees more with the experimentally observed one than the LDA level (PZ) results up to approximately 25 THz. In the case of the high-frequency doublet, the NNPscan calculations yielded a systematic shift by up to 1.5 THz with respect to the experimental VDOS. This shift is similar to that observed above for the α -cristobalite VDOS. Therefore, it is expected that the systematically underestimated vibrational frequencies arise from the limitation of the DFT reference method. In contrast, the PZ VDOS for silica glass agree well with the experimental data. This agreement is surprising given the rather higher deviation (up to 3 THz) of PZ VDOS from experimental VDOS for α -cristobalite. Hence, it can be assumed that the good agreement of the PZ results for vitreous silica is connected with an error cancellation due to the limited size of the amorphous silica model used in Ref. 61 (72 atoms). In contrast, the NNPscan calculations in this work used a 192 atom unit cell providing reproducible results from independent simulated annealing runs (see supplementary Figure S3). In summary, the novel NNPs can accurately model equilibrium structures and properties with DFT accuracy and in good agreement with experimental observations.

2.4 Phase transitions

Apart from close to equilibrium properties, considering high-energy parts of the PES including transition states is indispensable for simulations of phase transitions and the thermal stability of zeolites potentially leading to the discovery of new zeolites. To showcase the accuracy of the new NNPs for the description of reactive events the Stone-Wales defect formation⁶⁴ in a silica bilayer was chosen as a test case. In the following, we also compare PBE+D3 and SCAN+D3 results to quantify DFT accuracy. Figure 4 depicts the reaction path for Stone-Wales defect formation along with DFT and NNP energies (cf. Methods section). The bilayer structure is similar to the hypothetical bilayer structure in the reference dataset which consists of four, five, six and ten-membered rings (cf. Fig. S8c). However, no transition states from a six to seven-ring topology were included in the training set. Nonetheless, the NNPs show excellent agreement with their DFT reference. NNPs_{pbe} and NNPs_{scan} deviate less than 0.207 eV and 0.398 eV from the corresponding DFT values, which is about 4% of the highest barrier. For comparison, the PBE+D3 underestimates B3LYP results up to 0.665 eV and SCAN+D3 shows higher energies with a maximum deviation of 0.593 eV. These results show that the trained NNPs retains the reference method accuracy.

Achieving general modeling of reactive and non-reactive zeolite phase transitions beyond the model reaction path described above requires diverse configurations of the high-energy parts of the PES. Two extreme cases of phase transformations were considered to probe the quality of the PES interpolation between the low-energy EQ and high-energy transition states, *i.e.*, via Si-O bond cleavage (cf. Section 4.3): the melting and annealing of amorphous (AM) silica and zeolite amorphization (ZA). Figure 5 shows the relative energies with respect to α -quartz for simulations using the NNPs including the melting of β -cristobalite and the amorphization of LTA and FAU. Note that simulations of β -cristobalite melting and LTA amorphization up to mass density of 2.2 g/cm³ (22 Si/nm³) were used for training and active learning procedure, however, these simulations were carried out with different potentials, either ReaxFF or the initial NNPs (see Method section). Figure

5 also depicts results of DFT single-point calculations performed for a subset of structures as accuracy checks.

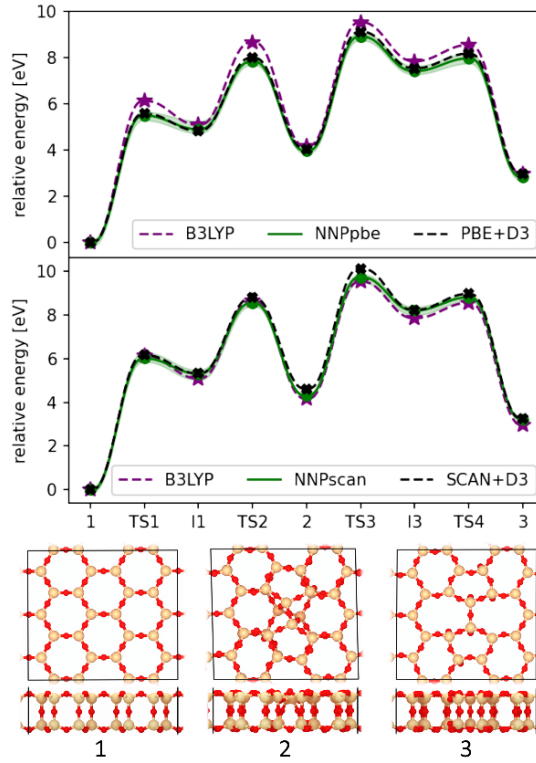


Figure 4: Energies of Stone-Wales defect formation calculated at the DFT (B3LYP taken from Ref. 64) and NNP level. Shaded areas indicate the energy range calculated with all six NNPs (solid line: ensemble average).

During the first $0.5 \cdot 10^6$ timesteps of the β -cristobalite melting simulation at 4800 K, only a few defects were created. The steep increase of the energy at about $0.6 \cdot 10^6$ timesteps corresponds to the phase transition into liquid silica. After 10^6 timesteps, the temperature was lowered stepwise down to 2500 K with no considerable changes in the structure during the last 100 000 timesteps. Again, NNP and DFT results show excellent agreement. In fact, similar to the results for the Stone-Wales defect formation energies, the difference between the two density functionals is much larger than between the NNP and the reference DFT, in particular at 4800 K (first 10^6 timesteps). The maximum energy difference between PBE+D3 and SCAN+D3 is about 128 meV/atom, while the

NNPs show a deviation of less than 27 meV/atom to their respective DFT reference.

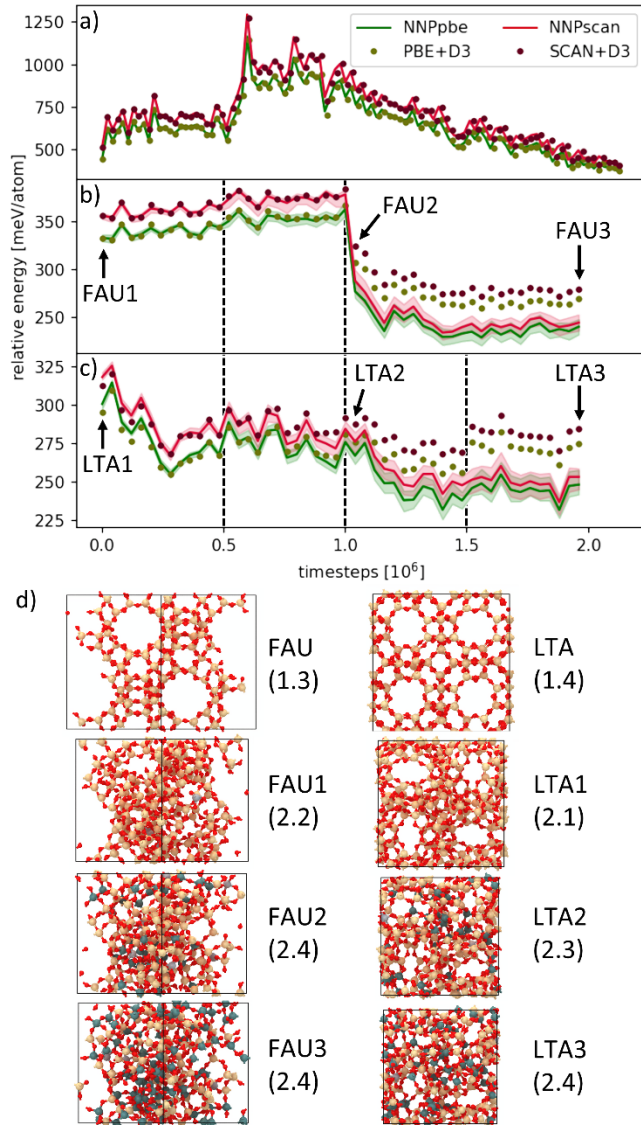


Figure 5: Comparison of DFT and NNP energies for (a) melting and annealing of β -cristobalite as well as amorphization of (b) FAU and (c) LTA by compression. Shaded areas in (a-c) show the energy range of all six NNPs (not visible in (a) due to energy scale) and dashed lines in (b-c) indicate compression steps. Structures and mass densities (in brackets) are depicted in (d). Si: yellow, O: red, Si (after bond breaking): green.

In contrast to the melting of glass, thermal zeolite amorphization involves not only Si-O bond

breaking but also considerable volume changes during the collapse of the framework. To mimic the thermal collapse of LTA and FAU, the structures were equilibrated at 1200 K for 6.5 ns with a stepwise volume reduction every 500 ps such that after 12 equivalent volume steps a mass density of 2.4 g/cm³ (24 Si/nm³) was reached (*cf.* Method section). The target density exceeds the density range of the configurations in the AM and ZA part of the reference dataset by about 10% to demonstrate the NNP accuracy in extrapolated regions of the PES. Figure 5b and 5c show the energies of the last $2 \cdot 10^6$ timesteps of the trajectories. Figure 5d depicts example structures taken from the MD trajectory. Note that FAU was not included in reference database. In addition, the equilibration time of the last volume step was 1 ns in the case of FAU to ensure full equilibration in the final stage of the framework collapse.

FAU shows no Si-O bond breaking up to the density of amorphous silica (2.2 g/cm³). However, the microporous structure considerably changes, mainly due to the collapse of the large cages. Starting from a mass density of 2.4 g/cm³, the trajectories of FAU show Si-O bond breakage and reformation events during the last 10^6 timesteps. The transition states are five-fold coordinated Si leading to cleavage of Si-O bonds and reorientation of SiO₄ tetrahedra. The same bond cleavage mechanism was obtained for LTA. However, the first bond breaking was obtained at a density of 2.1 g/cm³ as indicated by the energy drop in Fig. 5c.

Up to a density of 2.2 g/cm³ the deviation of both NNPpbe and NNPs can from their DFT reference (less than 11 meV/atom) is lower compared to difference between PBE+D3 and SCAN+D3 (up to 25 meV/atom). At densities above 2.2 g/cm³ larger NNP errors (up to 40 meV/atom) were obtained, while difference between PBE+D3 and SCAN+D3 remains approximately constant. The larger NNP errors are also indicated by the increased spread of the energy predictions of the NNP ensemble enabling future refinement of the NNPs by active learning. In fact, the energy spread of the NNP ensemble qualitatively correlates with the difference between the NNP ensemble average and the corresponding DFT reference with a Pearson correlation coefficient of about 0.8 (see supplementary

Figure S5). In addition, the NNP energies qualitatively agree with the DFT results (Pearson correlation coefficient about 0.99 and 0.8 for FAU and LTA, respectively, *cf.* Fig. S6) providing reasonable atomic configurations even in extrapolated regions at densities about 10% above the reference data. This facilitates a robust sampling of the configuration space for further active learning and NNP refinement.

3. Discussion

Energy errors of a few meV/atom and force errors of about 100-300 meV/Å have been reported previously for state-of-the-art MLP such as moment tensor or Gaussian approximation potentials trained for large-scale simulations of different materials.^{36,43-45} Results reported herein show that SchNet NNPs provide the same quality as other MLPs not only for close-to-equilibrium structures of materials but also for high-energy bond-breaking scenarios. In addition, we have demonstrated that the trained SchNet NNPs retain DFT accuracy and provide at least an order of magnitude higher accuracy compared to analytical force fields and tight binding DFT.

Previous trained reactive NNPs for silica⁴⁶ used a DFT database containing only two polymorphs (quartz and cristobalite), two surface structures, amorphous, and liquid silica configurations with unit cells comprising less than 144 atoms. The NNPs of Behler and Parrinello show RMSEs of about 200 meV/Å for forces, *i.e.*, somewhat higher compared to the RMSE of the database test set used in this work (147 meV/Å, *cf.* supplementary Table S4). The DFT database used in this work covers several low- and high-density polymorphs, 2D models, amorphous structures, and the large structural diversity of zeolites using unit cells with up to 400 atoms, including high-energy transition states (*cf.* Figure S8). Therefore, the NNPs provided in this work aim for a far more general modeling of the silica PES compared to previous studies⁴⁶ using only a small number of dense polymorphs, surface models, and amorphous silica structures.

The glass melting simulations clearly demonstrated the excellent NNP modeling accuracy for

bond-breaking events at 4800 K. During the equilibration at such high temperatures, the MD trajectory showed numerous five-fold coordinated transition states of Si in good agreement with DFT results. These MD simulations were performed using silica glass density (2.2 g/cm³) covered by the reference dataset containing configurations with densities from about 1.6 g/cm³ to 2.2 g/cm³ (16-22 Si/nm³) for high-energy transition states and densities from 1.0 to about 4.5 g/cm³ (10-45 Si/nm³) for low-energy EQ structures.

For comparison, the density range of the simulated zeolite collapse was 1.3 to 2.4 g/cm³. At densities below 2.2 g/cm³, MD simulations showed bond-breaking events in the case of LTA (2.1-2.2 g/cm³) and no bond cleavage in FAU. For both zeolites, the NNP energies and forces showed no extrapolation and agreed well with DFT results at densities lower than 2.2 g/cm³. Note that FAU was not part of the reference database. Only further compression to artificially high densities up to 10% beyond silica glass density resulted in NNP extrapolation. However, the difference between NNP and DFT energies was even in the extrapolation region at least three times lower (<40 meV/atom) than the RMSEs of the other PES approximations (e.g., 136 meV/atom for ReaxFF) shown in Table 1. In addition, the MD trajectories contain physically reasonable configurations allowing straightforward extension of the DFT dataset and further NNP refinement. Hence, these ZA simulations demonstrate that the SchNet NNPs are transferable and reasonably data-efficient interpolators of the silica PES as exemplified by qualitatively correct description of zeolite amorphization even slightly beyond the interpolation region.

The employed ZA simulation protocol only mimics the thermal zeolite collapse and does not provide realistic modeling of this phase transition. In fact, there are no reports of the thermal collapse for purely siliceous LTA and FAU. Most experimental studies on such phase transformations used Al-containing zeolites showing that zeolites with Si/Al ratios higher than 4 are thermally very stable due to the higher energetic barrier for breaking Si-O bonds than Al-O bonds.^{28,32} Therefore, the ZA simulations required artificial compression to higher densities to obtain a higher degree of

amorphization. However, even at lower densities ($< 2.2 \text{ g/cm}^3$), the ZA simulations showed bond-breaking events in LTA without extrapolation and in agreement with DFT results. These results demonstrate that the NNPs also reliably interpolate reactive parts of the PES that are relevant for transformations between different zeolite structures.

In summary, the trained NNPs allow general and accurate modeling of siliceous zeolites with DFT accuracy. This includes modeling of thermodynamic stabilities, equilibrium properties as well as reactive and non-reactive phase transitions of zeolites by interpolation of all *relevant* parts of the PES. Even in the observed cases of extrapolation, the NNPs showed qualitative agreement with DFT results with energy errors far lower than analytical force fields demonstrating the robustness of SchNet NNPs that allows their straightforward refinement and extension by active learning. Thanks to active learning, the NNPs capture the structural diversity of zeolites that is used for re-optimization of the Deem database with unprecedented accuracy. The revised database provides vital input for future machine learning studies on structure-stability-property correlations facilitating the computational – *in silico* – design and discovery of zeolites. Finally, NNP extension for modeling zeolites containing heteroatoms such as Al or guest molecules such as water is a promising route towards realistic atomistic modeling of zeolites under synthesis and operating conditions²⁷ with *ab initio* accuracy.

4. Methods

4.1 Dataset generation

Generation of the initial DFT datasets used PBE+D3 single-point calculations applied to a diverse set of structures, including silica polymorphs, surface models, hypothetical, and existing zeolites. First, ten hypothetical zeolites were selected from the Deem database by Farthest Point Sampling (FPS)^{65,66} to find the most diverse subsample of atomic environments. The FPS employed the similarity distance metric $d(A, B)$ between two zeolites A, B calculated using the average similarity

Kernel $\bar{K}(A, B)$ of the smooth overlap of atomic positions (SOAP)⁶⁷ descriptor (see supplementary information):⁶⁸

$$d(A, B) = \sqrt{2 - 2\bar{K}(A, B)}. \quad (1)$$

Apart from the ten selected zeolites, the FPS detected a hypothetical silica bilayer *in vacuo* (72 atoms, 12 Å vacuum layer), which was also added to the dataset (*cf.* Fig. S8c). Additionally, the dataset included a hypothetical α -quartz (001) surface model (120 atoms, 15 Å vacuum layer) terminated with dangling Si-O bonds. The dataset also contained five existing zeolites (CHA, SOD, IRR, MVY, MTF) and six silica polymorphs (α -quartz, α -cristobalite, tridymite, moganite, coesite, and stishovite) for consideration realistic silica structures.

All selected configurations were optimized at the PBE+D3 level under zero pressure conditions. Next, 210 different unit cell deformations were applied to all optimized structures (see supplementary information). Further sampling of atomic environments close to the optimized configurations used ten ps MD equilibrations (ReaxFF level) at 600 K and 1200 K. The 200 most diverse structures were extracted from every MD trajectory by the FPS described above. The resulting set of structures constitutes the low-energy, close to equilibrium (EQ) part of the silica database (*cf.* Fig. S8).

Sampling of high-energy configurations and transition states used MD simulations (ReaxFF level) for melting and simulating annealing of β -cristobalite (2×2×2 supercell). After scaling its mass density from 2.3 to 2.2 g/cm³ (silica glass density) and geometry optimization, the structure was equilibrated for 100 ps at 6000 K. Next, the temperature was reduced to 3000 K in three steps along with an equilibration for 100 ps at each temperature step. The equilibration at 3000 K used additional 100 ps to improve the structural sampling. Again, FPS was applied to the MD trajectories to find the 1000 most diverse configurations. To generate low-energy amorphous structures, ten configurations from the 3000 K MD trajectory were optimized (quenched) at constant volume (PBE+D3 level). The

lowest energy structure obtained was optimized under zero pressure conditions. Subsequently, the 210 lattice deformations used above (see supplementary information) were applied to the fully optimized unit cell. Structures generated from the simulated annealing of β -cristobalite are denoted as amorphous silica (AM) in the reference database (*cf.* Fig. S8).

In contrast to the melting of silica polymorphs, low-density zeolites show a significant volume contraction during melting, that is, thermal collapse. To mimic this process, eight hypothetical zeolites were equilibrated at 1200 K for 100 ps employing ReaxFF. Then, the unit cell volume was scaled stepwise such that after ten equivalent steps, the mass density of silica glass (2.2 g/cm³) was reached. After each contraction step, the zeolites were equilibrated for 100 ps. FPS of the resulting trajectories located 1000 diverse structures for each zeolite that fall into the zeolite amorphization (ZA) category of the dataset (*cf.* Fig. S8).

Single-point calculations at the PBE+D3 level were applied to the initial database providing energies and forces for the training of an ensemble of six NNPs allowing their iterative refinement.

4.2 NNP refinement

Refinement of the initially trained NNP ensemble requires extrapolation detection for previously unseen configurations. This is achieved by performing simulations using one leading NNP and applying single-point calculations to the trajectory using the remaining five potentials.³³ If the energy and force predictions deviate by more than 10 meV/atom or 750 meV/Å, respectively, from the NNP ensemble average, additional PBE+D3 single-point calculations were added to the reference database. Simulations and re-training of the NNP ensemble were repeated until no extrapolation was detected during test simulations.

To enhance the structural diversity of the EQ dataset, the Deem (331 171 structures, www.hypotheticalzeolites.net, accessed: November 29, 2019) and IZA (235 fully connected frameworks) databases were optimized using constant (zero) pressure conditions. Additionally, β -

cristobalite was equilibrated at 4800 K for 1 ns to sample more liquid silica configurations (AM). Extension of the ZA dataset used the same computational protocol for the thermal collapse (up to 2.2 g/cm³) of zeolites described above but for the frameworks LTA and SOD, which were not considered in the initial ZA dataset. The resulting PBE+D3 dataset contains 32952 structures with up to 400 atoms per unit cell. Single point calculations at the SCAN+D3 level were also applied to the final database to train the NNPscan potentials. More details on the DFT database are summarized in the supplementary information (Figures S7 and S8).

Training of NNP_{pbe} and NNP_{scan} used energy and forces of the databases calculated at the PBE+D3 and SCAN+D3 levels, respectively. The resulting test RMSE are approximately 4.7 meV/atom for energies and 147 meV/Å for forces (*cf.* supplementary Table S4). These errors are about an order of magnitude lower compared to other methods approximating the PES of silica (*cf.* Section 2.1).

4.3 Test simulations

The final geometry optimization of the Deem and IZA database was performed at the NNP_{scan} level. To test the NNP quality for reactive events, structures of the Stone-Wales defect formation were taken from Ref. 64. The unit cell parameters were optimized at the NNP_{scan} and NNP_{pbe} level keeping the fractional coordinates and the vacuum layer frozen, followed by DFT single-point calculations using the optimized structures. MD simulations (timestep 1 fs, NNP_{scan} level) of the thermal LTA and FAU collapse served as a test case of the final NNPs (FAU was not part of the final reference dataset). These simulations used the same procedure described above, but with 12 compression steps up to a mass density of 2.4 g/cm³ and an equilibration time of 500 ps between each step.

Test simulations (NNP_{scan} level) for the annealing of amorphous silica used three different initial structures: β -cristobalite and two vitreous silica structures taken from the ReaxFF simulated

annealing described above. Melting of β -cristobalite employed an equilibration for 1 ns at 4800 K. After geometry optimization, the two amorphous structures were equilibrated for 1 ns at 4200 K due to their lower energetic barrier for transition to the liquid state. In all three cases, the temperature was stepwise decreased to 2500 K in 100 K steps and an equilibration time of 25 ps per temperature step. The last structures of the MD trajectories were optimized under zero pressure conditions. The obtained glass configurations were equilibrated for 10 ps at 300 K (NVT ensemble), followed by another 10 ps equilibration using the NVE ensemble. Calculation of the VDOS used the velocity auto-correlation function from the NVE trajectory. In the case of α -cristobalite, the harmonic VDOS was calculated at the NNPscan and SCAN+D3 level using a $3\times 3\times 2$ supercell and the finite-difference (FD) approach. In addition, calculation of the anharmonic α -cristobalite VDOS at the NNPscan level employed MD simulations at 300 K with the same computational protocol used for the silica glass structures.

4.4 Computational details

DFT simulations at the GGA (PBE)⁶⁹ and meta-GGA (SCAN)⁷⁰ level employed the Vienna Ab initio Simulation Package (VASP, version 5.4.4)⁷¹⁻⁷⁴ along with the Projector Augmented-Wave (PAW) method.^{75,76} Calculations at constant volume used a plane-wave energy cutoff of 400 eV while the constant pressure optimizations used cutoff of 800 eV. The \mathbf{k} -point grids had a linear density of at least one \mathbf{k} -point per 0.1 \AA^{-1} along the reciprocal lattice vectors. Since consideration of long-range dispersion interactions is essential for accurate modeling of zeolites,⁷⁷⁻⁷⁹ the dispersion correction of Grimme *et al.* (D3)⁸⁰ with Becke-Johnson damping⁸¹ was added.

Training of SchNet⁴⁰ NNPs employed the Python package SchNetPack⁴¹ and random splits of the reference datasets into training, validation, and test sets at a ratio of 8:1:1. Mini-batch gradient descent optimization was applied for training along with a mini-batch size of eight structures and the ADAM optimizer.⁸² During NNP training the learning rate lowered stepwise (from 10^{-4} to 10^{-6}) by a

factor of 0.5 if the validation loss shows no improvement after 15 epochs. We used the same squared loss function for energy and forces as in Ref. 40 along with a trade-off factor of 0.01, that is, with high weight on force errors. The setup of the NNP hyper-parameters used six interaction blocks, 128-dimensional feature vectors, a cutoff radius 6 Å and a grid of 60 Gaussians for expansion of pairwise distances as input for the filter generating networks. A similar training and hyper-parameter setup provided very good NNP accuracy and training performance in previous works.^{40,41}

Calculations with the trained NNPs employed the atomic simulation environment (ASE).⁸³ Simulations at the ReaxFF⁵¹ level used the large-scale atomic/molecular massively parallel simulator (LAMMPS)^{84,85} and in the case of the Sanders-Leslie-Catlow (SLC) potential^{49,50} the General Utility Lattice Program (GULP).⁸⁶ GFN0-xTB⁵² calculations were performed with the xTB program package (version 6.3.3).⁸⁷

Unless stated otherwise, all MD simulations used a time step of 0.5 fs and the canonical (NVT) ensemble with the Nosé-Hoover thermostat.^{88,89} Calculation of the harmonic VDOS at the SCAN+D3 and NNPs can level employed the finite-difference (frozen-phonon) approach implemented in Phonopy⁹⁰ along with displacements of 0.02 Å. The VDOS calculations from MD trajectories used the Python package pwtools.⁹¹ Calculations of the SOAP descriptor were performed with the Python package Dscribe.⁹²

5. Data availability

The Deem and IZA database, the trained NNPs, and the test set used for accuracy evaluation is openly available in a Zenodo repository (<https://doi.org/10.5281/zenodo.5827897>). The remaining data for the reproduction of results is available upon reasonable request.

Acknowledgments

The authors acknowledge Charles University Centre of Advanced Materials (CUCAM) (OP VVV Excellent Research Teams, project number CZ.02.1.01/0.0/0.0/15_003/0000417) and the support of Primus Research Program of the Charles University (PRIMUS/20/SCI/004). PN acknowledges the Czech Science Foundation (grant No. 19-21534S). LG acknowledges the support of the Czech Science Foundation (20-26767Y).

This work was supported by The Ministry of Education, Youth and Sports from the Large Infrastructures for Research, Experimental Development and Innovations project „e-Infrastructure CZ – LM2018140“.

References

1. Li, Y., Li, L. & Yu, J. Applications of Zeolites in Sustainable Chemistry. *Chem* **3**, 928–949 (2017).
2. Akporiaye, D. E. & Price, G. D. Systematic enumeration of zeolite frameworks. *Zeolites* **9**, 23–32 (1989).
3. Deem, M. W., Pophale, R., Cheeseman, P. A. & Earl, D. J. Computational Discovery of New Zeolite-Like Materials. *J. Phys. Chem. C* **113**, 21353–21360 (2009).
4. Pophale, R., Cheeseman, P. A. & Deem, M. W. A database of new zeolite-like materials. *Phys. Chem. Chem. Phys.* **13**, 12407 (2011).
5. Blatov, V. A., Ilyushin, G. D. & Proserpio, D. M. The Zeolite Conundrum: Why Are There so Many Hypothetical Zeolites and so Few Observed? A Possible Answer from the Zeolite-Type Frameworks Perceived As Packings of Tiles. *Chem. Mater.* **25**, 412–424 (2013).
6. Baerlocher, Ch., Meier, W. M. & Olson, D. M. *Atlas of Zeolite Framework Types*. (Elsevier, Amsterdam, 2001).
7. Baerlocher, Ch. & McCusker, L. B. *Database of Zeolite Structures*: <http://www.iza-database.org>

structure.org/databases/ (accessed: February 20, 2020).

- 8. Mazur, M. *et al.* Synthesis of ‘unfeasible’ zeolites. *Nat. Chem.* **8**, 58–62 (2016).
- 9. Čejka, J., Morris, R. E., Nachtigall, P. & Roth, W. J. Layered inorganic solids. *Dalton Trans.* **43**, 10274 (2014).
- 10. Eliášová, P. *et al.* The ADOR mechanism for the synthesis of new zeolites. *Chem. Soc. Rev.* **44**, 7177–7206 (2015).
- 11. Firth, D. S. *et al.* Assembly–Disassembly–Organization–Reassembly Synthesis of Zeolites Based on *cfi* -Type Layers. *Chem. Mater.* **29**, 5605–5611 (2017).
- 12. Gatta, G. D. & Lee, Y. Zeolites at high pressure: A review. *Mineral. Mag.* **78**, 267–291 (2014).
- 13. Jordá, J. L. *et al.* Synthesis of a Novel Zeolite through a Pressure-Induced Reconstructive Phase Transition Process. *Angew. Chem. Int. Ed.* **52**, 10458–10462 (2013).
- 14. Thibaud, J.-M. *et al.* High-Pressure Phase Transition, Pore Collapse, and Amorphization in the Siliceous 1D Zeolite, TON. *J. Phys. Chem. C* **121**, 4283–4292 (2017).
- 15. Alberti, A., Cruciani, G. & Martucci, A. Reconstructive phase transitions induced by temperature in gmelinite-Na zeolite. *Am. Mineral.* **102**, 1727–1735 (2017).
- 16. Mazur, M. *et al.* Pressure-induced chemistry for the 2D to 3D transformation of zeolites. *J. Mater. Chem. A* **6**, 5255–5259 (2018).
- 17. Foster, M. D., Delgado Friedrichs, O., Bell, R. G., Almeida Paz, F. A. & Klinowski, J. Chemical Evaluation of Hypothetical Uninodal Zeolites. *J. Am. Chem. Soc.* **126**, 9769–9775 (2004).
- 18. Li, Y., Yu, J. & Xu, R. Criteria for Zeolite Frameworks Realizable for Target Synthesis. *Angew. Chem. Int. Ed.* **52**, 1673–1677 (2013).
- 19. Zimmermann, N. E. R. & Haranczyk, M. History and Utility of Zeolite Framework-Type Discovery from a Data-Science Perspective. *Cryst. Growth Des.* **16**, 3043–3048 (2016).
- 20. Perez, J. L. S., Haranczyk, M. & Zimmermann, N. E. R. High-throughput assessment of hypothetical zeolite materials for their synthesizability and industrial deployability. *Z. Für*

Krist. - Cryst. Mater. **234**, 437–450 (2019).

21. Akporiaye, D. E. & Price, G. D. Relative stability of zeolite frameworks from calculated energetics of known and theoretical structures. *Zeolites* **9**, 321–328 (1989).
22. Henson, N. J., Cheetham, A. K. & Gale, J. D. Theoretical Calculations on Silica Frameworks and Their Correlation with Experiment. *Chem. Mater.* **6**, 1647–1650 (1994).
23. Moliner, M., Román-Leshkov, Y. & Corma, A. Machine Learning Applied to Zeolite Synthesis: The Missing Link for Realizing High-Throughput Discovery. *Acc. Chem. Res.* **52**, 2971–2980 (2019).
24. Schwalbe-Koda, D., Jensen, Z., Olivetti, E. & Gómez-Bombarelli, R. Graph similarity drives zeolite diffusionless transformations and intergrowth. *Nat. Mater.* **18**, 1177–1181 (2019).
25. Evans, J. D. & Coudert, F.-X. Predicting the Mechanical Properties of Zeolite Frameworks by Machine Learning. *Chem. Mater.* **29**, 7833–7839 (2017).
26. Lee, S., Kim, B. & Kim, J. Predicting performance limits of methane gas storage in zeolites with an artificial neural network. *J. Mater. Chem. A* **7**, 2709–2716 (2019).
27. Grajciar, L. *et al.* Towards operando computational modeling in heterogeneous catalysis. *Chem. Soc. Rev.* **47**, 8307–8348 (2018).
28. Peral, I. & Íñiguez, J. Amorphization Induced by Pressure: Results for Zeolites and General Implications. *Phys. Rev. Lett.* **97**, 225502 (2006).
29. Wondraczek, L. *et al.* Kinetics of Decelerated Melting. *Adv. Sci.* **5**, 1700850 (2018).
30. Greaves, G. N. *et al.* The rheology of collapsing zeolites amorphized by temperature and pressure. *Nat. Mater.* **2**, 622–629 (2003).
31. Greaves, G. N. *et al.* Zeolite collapse and polyamorphism. *J. Phys. Condens. Matter* **19**, 415102 (2007).
32. Cruciani, G. Zeolites upon heating: Factors governing their thermal stability and structural changes. *J. Phys. Chem. Solids* **67**, 1973–1994 (2006).

33. Behler, J. First Principles Neural Network Potentials for Reactive Simulations of Large Molecular and Condensed Systems. *Angew. Chem. Int. Ed.* **56**, 12828–12840 (2017).
34. Mueller, T., Hernandez, A. & Wang, C. Machine learning for interatomic potential models. *J. Chem. Phys.* **152**, 050902 (2020).
35. von Lilienfeld, O. A., Müller, K.-R. & Tkatchenko, A. Exploring chemical compound space with quantum-based machine learning. *Nat. Rev. Chem.* **4**, 347–358 (2020).
36. Zuo, Y. *et al.* Performance and Cost Assessment of Machine Learning Interatomic Potentials. *J. Phys. Chem. A* **124**, 731–745 (2020).
37. Keith, J. A. *et al.* Combining Machine Learning and Computational Chemistry for Predictive Insights Into Chemical Systems. Preprint at <http://arxiv.org/abs/2102.06321> (2021).
38. Lubbers, N., Smith, J. S. & Barros, K. Hierarchical modeling of molecular energies using a deep neural network. *J. Chem. Phys.* **148**, 241715 (2018).
39. Thomas, N. *et al.* Tensor field networks: Rotation- and translation-equivariant neural networks for 3D point clouds. Preprint at <http://arxiv.org/abs/1802.08219> (2018).
40. Schütt, K. T., Sauceda, H. E., Kindermans, P.-J., Tkatchenko, A. & Müller, K.-R. SchNet – A deep learning architecture for molecules and materials. *J. Chem. Phys.* **148**, 241722 (2018).
41. Schütt, K. T. *et al.* SchNetPack: A Deep Learning Toolbox For Atomistic Systems. *J. Chem. Theory Comput.* **15**, 448–455 (2019).
42. Novoselov, I. I., Yanilkin, A. V., Shapeev, A. V. & Podryabinkin, E. V. Moment tensor potentials as a promising tool to study diffusion processes. *Comput. Mater. Sci.* **164**, 46–56 (2019).
43. Rosenbrock, C. W. *et al.* Machine-learned interatomic potentials for alloys and alloy phase diagrams. *Npj Comput. Mater.* **7**, 1–9 (2021).
44. Sivaraman, G. *et al.* Machine-learned interatomic potentials by active learning: amorphous and liquid hafnium dioxide. *Npj Comput. Mater.* **6**, 104 (2020).

45. George, J., Hautier, G., Bartók, A. P., Csányi, G. & Deringer, V. L. Combining phonon accuracy with high transferability in Gaussian approximation potential models. *J. Chem. Phys.* **153**, 044104 (2020).

46. Li, W. & Ando, Y. Comparison of different machine learning models for the prediction of forces in copper and silicon dioxide. *Phys. Chem. Chem. Phys.* **20**, 30006–30020 (2018).

47. Liu, H., Fu, Z., Li, Y., Sabri, N. F. A. & Bauchy, M. Machine Learning Forcefield for Silicate Glasses. Preprint at <http://arxiv.org/abs/1902.03486> (2019).

48. Schran, C., Brezina, K. & Marsalek, O. Committee neural network potentials control generalization errors and enable active learning. *J. Chem. Phys.* **153**, 104105 (2020).

49. Sanders, M. J., Leslie, M. & Catlow, C. R. A. Interatomic potentials for SiO₂. *J. Chem. Soc. Chem. Commun.* 1271–1273 (1984) doi:10/bktzk2.

50. Schröder, K.-P. *et al.* Bridging hydroxyl groups in zeolitic catalysts: a computer simulation of their structure, vibrational properties and acidity in protonated faujasites (H□Y zeolites). *Chem. Phys. Lett.* **188**, 320–325 (1992).

51. Fogarty, J. C., Aktulga, H. M., Grama, A. Y., van Duin, A. C. T. & Pandit, S. A. A reactive molecular dynamics simulation of the silica-water interface. *J. Chem. Phys.* **132**, 174704 (2010).

52. Bannwarth, C. *et al.* Extended tight-binding quantum chemistry methods. *WIREs Comput. Mol. Sci.* **11**, e1493 (2021).

53. Bertels, L. W., Newcomb, L. B., Alaghemandi, M., Green, J. R. & Head-Gordon, M. Benchmarking the Performance of the ReaxFF Reactive Force Field on Hydrogen Combustion Systems. *J. Phys. Chem. A* **124**, 5631–5645 (2020).

54. Zheng, N. Microporous and Photoluminescent Chalcogenide Zeolite Analogs. *Science* **298**, 2366–2369 (2002).

55. Armstrong, J. A. & Weller, M. T. Berylliosilicate Frameworks and Zeolites. *J. Am. Chem. Soc.*

132, 15679–15686 (2010).

56. Piccione, P. M. *et al.* Thermochemistry of Pure-Silica Zeolites. *J. Phys. Chem. B* **104**, 10001–10011 (2000).
57. Wragg, D. S., Morris, R. E. & Burton, A. W. Pure Silica Zeolite-type Frameworks: A Structural Analysis. *Chem. Mater.* **20**, 1561–1570 (2008).
58. Wehinger, B. *et al.* Lattice dynamics of α -cristobalite and the Boson peak in silica glass. *J. Phys. Condens. Matter* **27**, 305401 (2015).
59. Buchenau, U. *et al.* Low-frequency modes in vitreous silica. *Phys. Rev. B* **34**, 5665–5673 (1986).
60. Guillot, B. & Guissani, Y. Boson Peak and High Frequency Modes in Amorphous Silica. *Phys. Rev. Lett.* **78**, 2401–2404 (1997).
61. Sarnthein, J., Pasquarello, A. & Car, R. Origin of the High-Frequency Doublet in the Vibrational Spectrum of Vitreous SiO₂. *Science* **275**, 1925–1927 (1997).
62. Tong, Z., Yang, X., Feng, T., Bao, H. & Ruan, X. First-principles predictions of temperature-dependent infrared dielectric function of polar materials by including four-phonon scattering and phonon frequency shift. *Phys. Rev. B* **101**, 125416 (2020).
63. Zhang, D.-B., Sun, T. & Wentzcovitch, R. M. Phonon Quasiparticles and Anharmonic Free Energy in Complex Systems. *Phys. Rev. Lett.* **112**, 058501 (2014).
64. Klemm, H. W. *et al.* A Silica Bilayer Supported on Ru(0001): Following the Crystalline-to-Vitreous Transformation in Real Time with Spectro-microscopy. *Angew. Chem. Int. Ed.* **59**, 10587–10593 (2020).
65. Eldar, Y., Lindenbaum, M., Porat, M. & Zeevi, Y. Y. The farthest point strategy for progressive image sampling. *IEEE Trans. Image Process.* **6**, 1305–1315 (1997).
66. Imbalzano, G. *et al.* Automatic selection of atomic fingerprints and reference configurations for machine-learning potentials. *J. Chem. Phys.* **148**, 241730 (2018).

67. Bartók, A. P., Kondor, R. & Csányi, G. On representing chemical environments. *Phys. Rev. B* **87**, 184115 (2013).

68. De, S., Bartók, A. P., Csányi, G. & Ceriotti, M. Comparing molecules and solids across structural and alchemical space. *Phys. Chem. Chem. Phys.* **18**, 13754–13769 (2016).

69. Perdew, J. P., Burke, K. & Ernzerhof, M. Generalized gradient approximation made simple. *Phys. Rev. Lett.* **77**, 3865–3868 (1996).

70. Sun, J., Ruzsinszky, A. & Perdew, J. P. Strongly Constrained and Appropriately Normed Semilocal Density Functional. *Phys. Rev. Lett.* **115**, 036402 (2015).

71. Kresse, G. & Hafner, J. Ab initio molecular dynamics for liquid metals. *Phys. Rev. B* **47**, 558–561 (1993).

72. Kresse, G. & Hafner, J. Ab initio molecular-dynamics simulation of the liquid-metal–amorphous-semiconductor transition in germanium. *Phys. Rev. B* **49**, 14251–14269 (1994).

73. Kresse, G. & Furthmüller, J. Efficient iterative schemes for *ab initio* total-energy calculations using a plane-wave basis set. *Phys. Rev. B* **54**, 11169–11186 (1996).

74. Kresse, G. & Furthmüller, J. Efficiency of ab-initio total energy calculations for metals and semiconductors using a plane-wave basis set. *Comput. Mater. Sci.* **6**, 15–50 (1996).

75. Blöchl, P. E. Projector Augmented-Wave Method. *Phys. Rev. B* **50**, 17953–17979 (1994).

76. Kresse, G. & Joubert, D. From ultrasoft pseudopotentials to the projector augmented-wave method. *Phys. Rev. B* **59**, 1758–1775 (1999).

77. Hay, H., Ferlat, G., Casula, M., Seitsonen, A. P. & Mauri, F. Dispersion effects in SiO₂ polymorphs: An *ab initio* study. *Phys. Rev. B* **92**, 144111 (2015).

78. Fischer, M., Kim, W. J., Badawi, M. & Lebègue, S. Benchmarking the performance of approximate van der Waals methods for the structural and energetic properties of SiO₂ and AlPO₄ frameworks. *J. Chem. Phys.* **150**, 094102 (2019).

79. Rehak, F. R., Piccini, G., Alessio, M. & Sauer, J. Including dispersion in density functional

theory for adsorption on flat oxide surfaces, in metal–organic frameworks and in acidic zeolites. *Phys. Chem. Chem. Phys.* **22**, 7577–7585 (2020).

80. Grimme, S., Antony, J., Ehrlich, S. & Krieg, H. A consistent and accurate ab initio parametrization of density functional dispersion correction (DFT-D) for the 94 elements H–Pu. *J. Chem. Phys.* **132**, 154104 (2010).

81. Grimme, S., Ehrlich, S. & Goerigk, L. Effect of the damping function in dispersion corrected density functional theory. *J. Comput. Chem.* **32**, 1456–1465 (2011).

82. Kingma, D. P. & Ba, J. Adam: A Method for Stochastic Optimization. Preprint at <http://arxiv.org/abs/1412.6980> (2017).

83. Larsen, A. H. *et al.* The atomic simulation environment—a Python library for working with atoms. *J. Phys. Condens. Matter* **29**, 273002 (2017).

84. Plimpton, S. Fast Parallel Algorithms for Short-Range Molecular-Dynamics. *J. Comput. Phys.* **117**, 1–19 (1995).

85. Aktulga, H. M., Fogarty, J. C., Pandit, S. A. & Grama, A. Y. Parallel reactive molecular dynamics: Numerical methods and algorithmic techniques. *Parallel Comput.* **38**, 245–259 (2012).

86. Gale, J. D. & Rohl, A. L. The General Utility Lattice Program (GULP). *Mol. Simul.* **29**, 291–341 (2003).

87. *Semiempirical Extended Tight-Binding Program Package xtb, Version 6.3.3*, <https://github.com/grimme-lab/xtb> (accessed: October 28, 2020).

88. Nosé, S. A Unified Formulation of the Constant Temperature Molecular Dynamics Methods. *J. Chem. Phys.* **81**, 511–519 (1984).

89. Hoover, W. G. Canonical Dynamics: Equilibrium Phase-Space Distributions. *Phys. Rev. A* **31**, 1695–1697 (1985).

90. Togo, A. & Tanaka, I. First principles phonon calculations in materials science. *Scr. Mater.*

108, 1–5 (2015).

91. *pwtools*, <https://github.com/elcorto/pwtools> (accessed: November 15, 2020).
92. Himanen, L. *et al.* Dscribe: Library of descriptors for machine learning in materials science. *Comput. Phys. Commun.* **247**, 106949 (2020).

Supplementary information

Accurate large-scale simulations of siliceous zeolites by neural network potentials

Andreas Erlebach¹, Petr Nachtigall¹, & Lukáš Grajciar^{1*}

¹*Department of Physical and Macromolecular Chemistry, Charles University, Hlavova 8, 128 43 Praha 2*

1. Accuracy evaluation

Table S1: Root mean square (RMSE) and mean absolute error (MAE) of energies [meV/atom] and forces [eV/Å] calculated for all test cases and only for equilibrium configurations (EQ) with respect to SCAN+D3 results. NNP results include calculations of a single potential (sNNP) and an ensemble of six NNPs (eNNP).

Level of theory	Energy (EQ)		Forces (EQ)		Energy (all)		Forces (all)	
	MAE	RMSE	MAE	RMSE	MAE	RMSE	MAE	RMSE
PBE+D3	2.34	2.89	0.128	0.186	16.1	31.5	0.171	0.233
sNNP ^{pbe}	3.89	5.08	0.131	0.182	15.8	29.0	0.242	0.356
	(2.51)	(3.36)	(0.044)	(0.064)	(3.65)	(5.25)	(0.162)	(0.283)
eNNP ^{pbe}	4.18	5.55	0.130	0.180	16.4	29.6	0.226	0.326
	(2.46)	(3.52)	(0.042)	(0.062)	(3.35)	(4.90)	(0.144)	(0.247)

The test set used for error calculation in Table 1 did not include the structures from the second half of the ZA simulations since these are considered to be in an extrapolation region of the configuration space with energy errors between ca. 20-40 meV/atom (cf. Fig. 5b and 5c). Table S2 also summarizes the errors for a test set that includes 50 additional structures from the extrapolated part of the ZA simulations.

Table S2: Root mean square (RMSE) and mean absolute error (MAE) of energies [meV/atom] and forces [eV/Å] calculated for all test cases including the extrapolated structures from the zeolite amorphization trajectory (cf. Fig. 5). Errors are given with respect to the SCAN+D3 calculations. NNPPbe errors with respect to PBE+D3 are given in parentheses. NNP results include calculations of a single potential (sNNP) and an ensemble of six NNPs (eNNP).

Level of theory	Energy (all)		Forces (all)	
	MAE	RMSE	MAE	RMSE
PBE+D3	16.0	31.0	0.174	0.235
sNNP ^{pbe}	16.7	29.6	0.274	0.400
	(4.53)	(7.72)	(0.203)	(0.345)
eNNP ^{pbe}	17.1	29.9	0.260	0.379
	(4.07)	(6.78)	(0.187)	(0.318)
sNNP ^{scan}	5.05	9.00	0.211	0.352
eNNP ^{scan}	4.70	7.85	0.196	0.330
SLC	211.2	313.9	3.255	4.201
ReaxFF	96.1	145.6	2.957	8.732
GFN0-xTB	127.2	199.3	0.738	3.241

2. Equilibrium properties

Figure S1 depicts the energy-density plots $E(\rho)$ (cf. Fig. 2) of the IZA database calculated using SLC and NNP^{scan}. It also shows the results of linear regression for 40 zeolites that exist in their purely siliceous form.¹ The obtained functions were shifted to indicate the accessible energy-density range of siliceous zeolite frameworks. NNP^{scan} optimizations resulted in considerably lower relative energies than the SLC level calculations, particularly for three-ring containing zeolites such as Beryllosilicates (OBW, NAB, JOZ, OSO).² However, the Beryllosilicates and the ‘unfeasible’ high silica zeolite IPC-10³ show relative energies above the accessible range of siliceous frameworks in both cases NNP^{scan} and SLC.

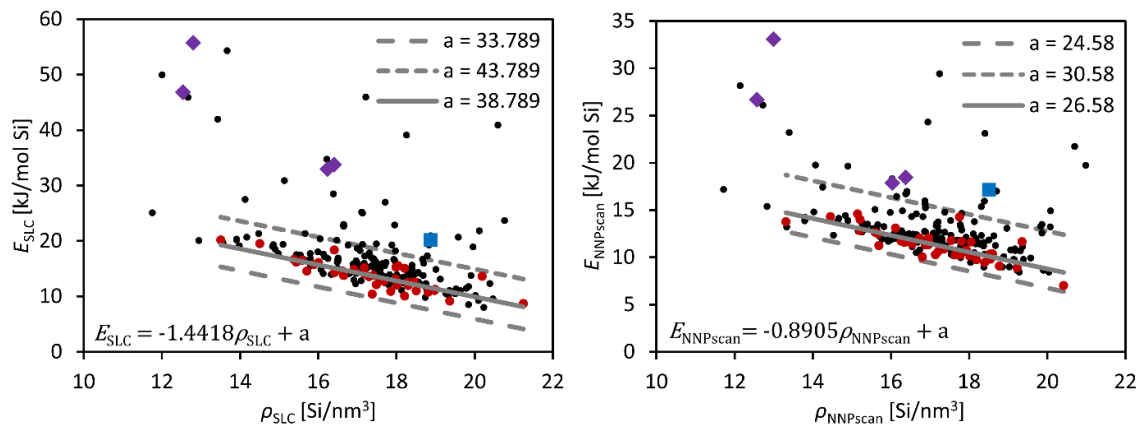


Figure S1: Relative energy E as a function of framework density ρ calculated at the SLC (left) and NNP^{scan} (right) level of the IZA database (black dots). The solid lines show the linear regression of $E(\rho)$ for 40 purely siliceous zeolites (red dots). The obtained linear functions $E(\rho)$ were shifted by ± 5 (SLC) and $-2/+4$ kJ/mol (NNP^{scan}) to define the accessible energy range of siliceous zeolites (dashed lines, cf. Fig. 2). Purple diamonds: Beryllosilicate zeolites (OBW, NAB, JOZ, OSO), blue square: IPC-10 (PCR).

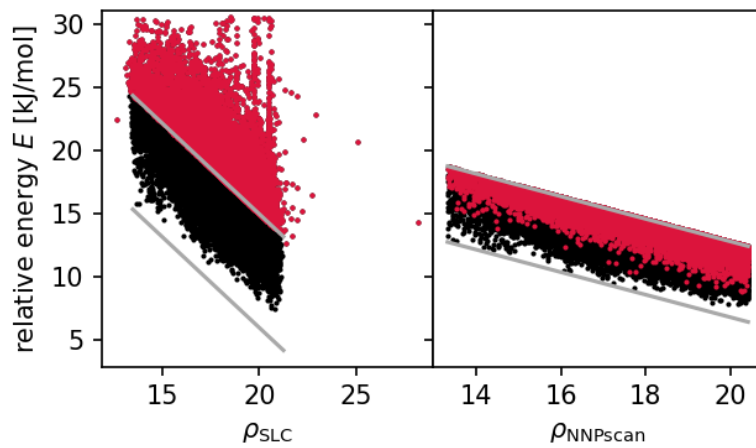


Figure S2: Relative energy E as a function of framework density ρ calculated at the SLC (left) and NNPscan (right) level. The solid lines indicate the thermodynamically accessible range of purely siliceous zeolites (cf. Figure 2 and S1). The black dots show the 32794 (SLC predicted) accessible frameworks. Red dots highlight the 20340 additional zeolites that are within the NNPscan predicted, thermodynamically accessible range of solvothermal synthesis routes.

Table S3: Relative energies ΔE [kJ/mol Si] and density ρ [Si/nm³] calculated at the DFT, NNP (single potential sNNP, ensemble average eNNP), and SLC level for α -quartz (qu), α -cristobalite (cr), tridymite (tri), moganite (mo), coesite (co), existing siliceous and one hypothetical (HYP) zeolite. Experimental values for relative enthalpies ΔH and densities were taken from Refs. 4–6. Mean absolute deviation (MAD) with respect to experimental values is given for all structures and a subset of structures optimized at the DFT level (MAD_{sub}).

	SLC		SCAN+D3		sNNPscan		eNNPscan		PBE+D3		sNNPpbe		eNNPpbe		EXP	
	ΔE	ρ	ΔH	ρ												
qu	0.00	27.74	0.00	26.96	0.00	26.99	0.00	26.87	0.00	25.92	0.00	25.11	0.00	25.72	0.00	26.52
cr	3.54	23.13	4.36	23.24	6.00	23.47	6.06	23.57	4.03	22.68	4.26	24.22	4.41	24.11	2.84	23.37
tr	5.41	21.91	7.08	22.17	6.42	21.75	6.44	21.62	6.49	21.61	7.07	21.75	6.70	21.42	3.21	22.61
mo	1.06	29.26	0.66	27.06	-0.36	27.04	-0.01	27.10	0.46	26.41	0.52	26.41	-0.10	26.39	3.40	26.22
co	1.96	30.90	2.03	29.43	1.36	29.41	1.44	29.46	3.26	28.65	3.24	28.73	2.85	28.68	2.93	29.26
AFI	12.10	17.49	11.38	17.16	10.27	17.14	9.61	17.48	12.04	16.89	11.58	16.77	10.84	16.75	7.20	16.90
FER	11.94	18.30	10.64	17.90	10.77	17.94	10.17	18.26	11.20	17.46	11.33	18.22	11.29	17.93	6.60	18.43
HYP	5.61	26.57	3.64	26.35	-0.46	26.34	-0.23	26.26	2.90	25.70	-0.59	25.50	-0.75	25.49	-	-
IFR	15.17	17.17	12.04	17.16	11.31	16.88	11.47	16.91	12.03	17.15	12.01	16.78	11.51	16.74	10.00	17.03
CFI	13.56	17.30	12.22	16.98	12.08	16.97	10.41	17.69	13.46	16.77	14.23	16.54	13.54	16.51	8.80	18.28
MTW	11.02	18.51	9.89	18.49	9.97	18.54	9.58	18.49	10.89	18.23	11.40	18.17	10.25	18.35	8.70	18.20
MEL	10.92	17.85	-	-	10.23	17.64	9.86	17.66	-	-	11.00	17.67	10.40	17.63	8.20	17.80
MWW	14.56	16.62	-	-	11.38	16.54	11.54	16.52	-	-	12.45	16.35	12.03	16.30	10.40	16.51
ITE	14.32	16.42	-	-	11.72	16.26	11.72	16.22	-	-	12.81	15.98	12.37	15.96	10.10	16.26
AST	18.35	16.41	-	-	13.09	16.12	12.29	16.93	-	-	15.22	15.76	12.84	16.96	10.90	17.29
STT	14.89	16.92	-	-	12.03	16.73	12.10	16.68	-	-	13.33	16.47	12.78	16.45	9.20	16.83
CHA	16.52	15.59	-	-	12.83	15.21	12.80	15.22	-	-	14.03	14.85	13.57	14.87	11.40	15.40
BEA	14.59	15.71	-	-	12.65	15.60	12.35	15.53	-	-	14.03	15.39	13.33	15.31	9.30	15.60
MFI	10.06	18.21	-	-	9.73	18.19	9.68	18.01	-	-	10.82	18.18	10.28	18.05	6.80	17.97
ISV	16.65	15.38	-	-	14.60	15.15	14.49	15.13	-	-	15.76	15.17	15.14	15.07	14.40	15.36
FAU	20.16	13.51	-	-	13.78	13.31	13.92	13.29	-	-	14.54	13.00	13.98	13.05	13.60	13.30
MAD_{sub}	3.19	0.90	2.66	0.45	2.76	0.49	2.36	0.44	2.90	0.57	3.08	0.62	2.75	0.63	-	-
MAD	3.97	0.55	-	-	2.24	0.35	1.99	0.28	-	-	3.02	0.51	2.50	0.46	-	-

Figure S3 shows the vibrational density of states (VDOS) of silica glass models obtained from three independent simulated annealing runs. The excellent agreement of all VDOS indicates that the simulation procedure yielded reliable and reproducible glass structure predictions.

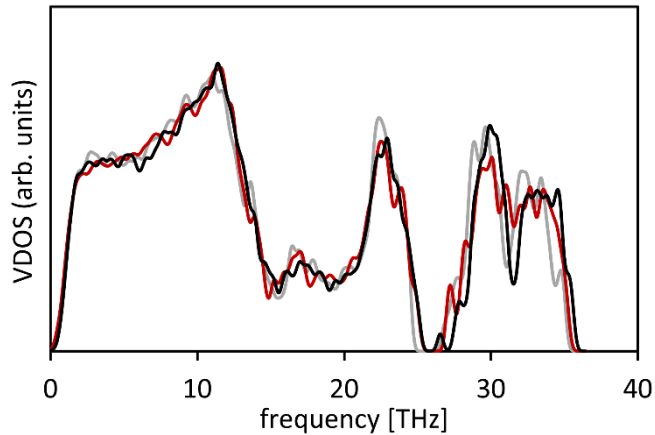


Figure S3: Vibrational density of states (VDOS) of amorphous silica structures obtained from three independent simulated annealing runs at the NNPscan level.

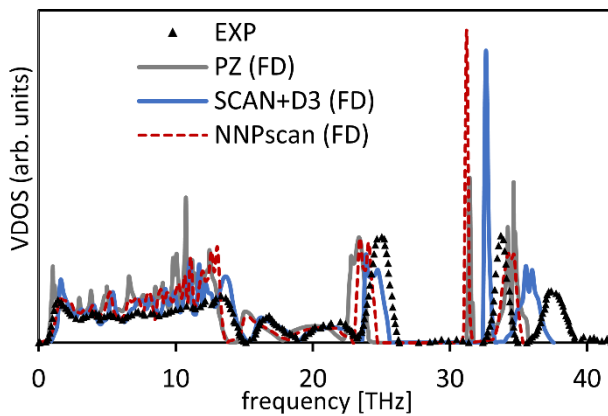


Figure S4: Vibrational density of states (VDOS) of α -cristobalite obtained from experiments (EXP), DFT (PZ and SCAN+D3) and NNPscan calculations using the finite-difference (FD) approach (*cf.* Figure 3).

3. Phase transitions

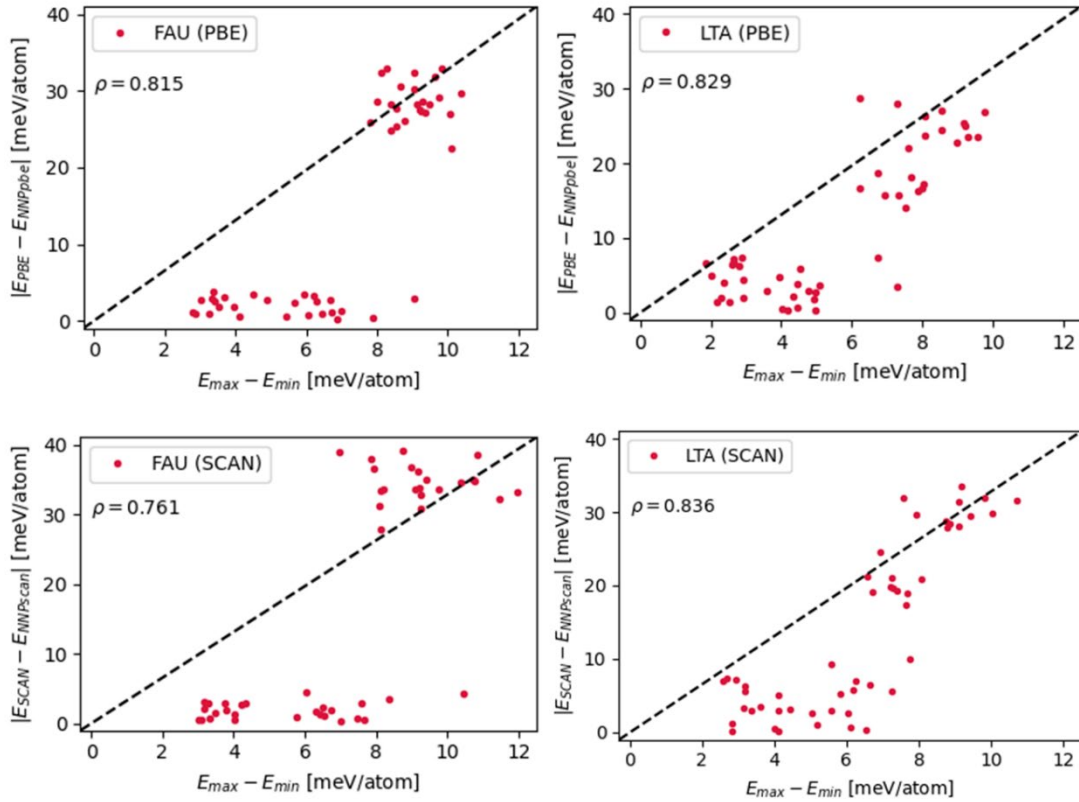


Figure S5: Qualitative correlation of NNP errors with the energy prediction spread (difference of max. and min. energy) of the NNP ensemble obtained from zeolite amorphization simulations (*cf.* Figure 5). Pearson correlation coefficients ρ for all cases are also given.

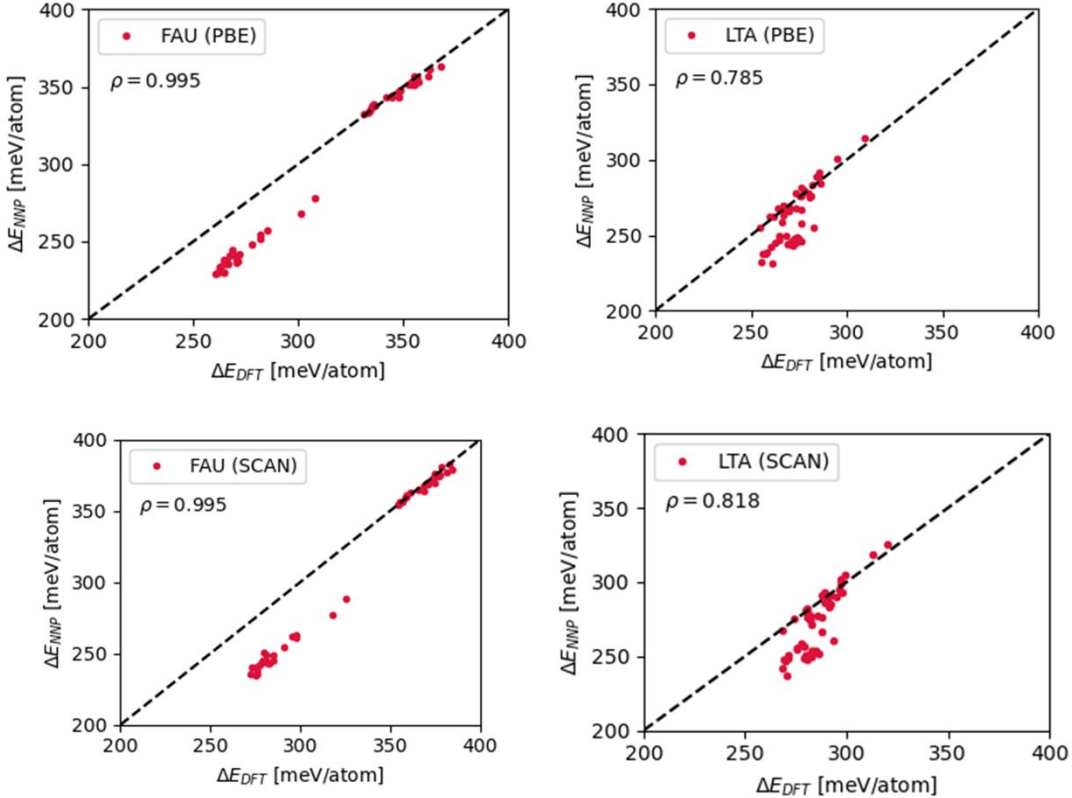


Figure S6: Qualitative correlation of relative NNP and DFT energies obtained from zeolite amorphization simulations (cf. Figure 5) along with Pearson correlation coefficients ρ .

4. Dataset generation

The selection of diverse zeolite frameworks from the Deem database used a subset of 69079 structures containing less than 80 atoms per unit cell. The selected subset covers the whole energy-density range of the full database (see Fig. S7a). To find diverse atomic environments in the subset, the applied farthest point sampling (FPS) used the smooth overlap of atomic positions (SOAP) descriptor as similarity metric.

Calculation of the SOAP power spectrum $\mathbf{p}(\chi_i^A)$ for n atomic environments χ_i^A in structure A used a cutoff $r_{\text{cut}} = 6 \text{ \AA}$, $n_{\text{max}} = 8$ radial basis functions (gaussian type orbitals) and spherical harmonics up to degree $l_{\text{max}} = 8$. A computationally efficient way to compare two different zeolites is the calculations of the average power spectrum over all atoms in the structure:

$$\hat{\mathbf{p}}(A) = \frac{1}{n} \sum_i^n \mathbf{p}(\chi_i^A). \quad (\text{S1})$$

The average SOAP similarity kernel $K(A, B)$ of two different structures A, B equals the dot product of the average power spectra $K(A, B) = \hat{\mathbf{p}}(A) \cdot \hat{\mathbf{p}}(B)$.^{7,8} Calculation of the similarity distance metric (eq 1) for the FPS used the normalized similarity kernel $\bar{K}(A, B)$:⁸

$$\bar{K}(A, B) = \frac{K(A, B)}{\sqrt{K(A, A)K(B, B)}}. \quad (\text{S2})$$

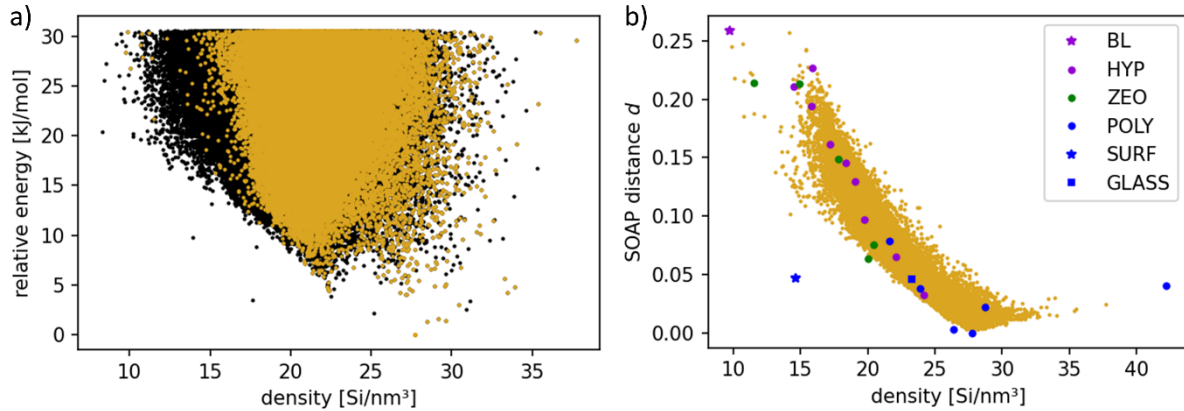


Figure S7: (a) Relative energy and (b) SOAP distance d (eq 1) with respect to α -quartz as a function of framework density of the Deem database (black dots) and a subset of structures containing less than 80 atoms per unit cell (yellow dots). The equilibrium structures selected for dataset generation are highlighted in (b): hypothetical (HYP) zeolites from FPS of the subset, existing zeolites (ZEO) and silica polymorphs (POLY), amorphous silica (GLASS), a silica bilayer (BL), and an α -quartz (001) surface model (SURF).

Fig. S7b shows the SOAP similarity distance (eq 1) as a function of framework density for hypothetical zeolites selected by FPS and existing zeolites, silica polymorphs, silica glass, an α -quartz surface, and a silica bilayer model. The chosen set of structures represents the diversity of densities and atomic environments of silica, ranging from low-density zeolites and surface models to high-density polymorphs such as coesite and stishovite.

To sample diverse configurations close to equilibrium (EQ), the selected structures were first optimized at the DFT level under constant (zero) pressure conditions. Next, DFT single-point calculations were applied to 210 different lattice deformations and 200 configurations extracted by FPS from MD trajectories (ReaxFF level) at 600 and 1200 K for every optimized structure. The deformed unit cells \mathbf{M}_d were obtained using $\mathbf{M}_d = (\mathbf{I} + \boldsymbol{\varepsilon})\mathbf{M}_0$ from the optimized unit cell matrix $\mathbf{M}_0 = (\mathbf{a}, \mathbf{b}, \mathbf{c})$ with the lattice vectors $\mathbf{a}, \mathbf{b}, \mathbf{c}$. The unit cell remains unchanged if the six independent elements ε_{ij} of the symmetric 3×3 matrix $\boldsymbol{\varepsilon}$ equal zero. There are 70 different permutations for lattice deformations ranging from one single $\varepsilon_{ij} = \pm d$ (rest zero) up to all six $\varepsilon_{ij} = \pm d$. Here, three deformation factors $d = 0.015, 0.03, 0.045$ were considered yielding 210 different lattice deformations.

The NNPs presented here are designed for accurate description of diverse atomic structures and densities of zeolites, covering also high-energy parts of the PES. This was achieved by iterative extension of an initial dataset and (re)training of an NNP ensemble using active learning (see Section 4.1 and 4.2). Figure S8 shows the relative energies with respect to α -quartz of the final zeolite database as a function of atomic density and the similarity distance metric d (eq 1) calculated using the smooth overlap of atomic positions (SOAP) descriptor. The database contains low-energy, close to equilibrium (EQ) structures and high-energy structures from phase transition simulations (*cf.* Section 2.4) at high temperatures (amorphous and liquid silica (AM)) and high pressures (zeolite amorphization (ZA)).

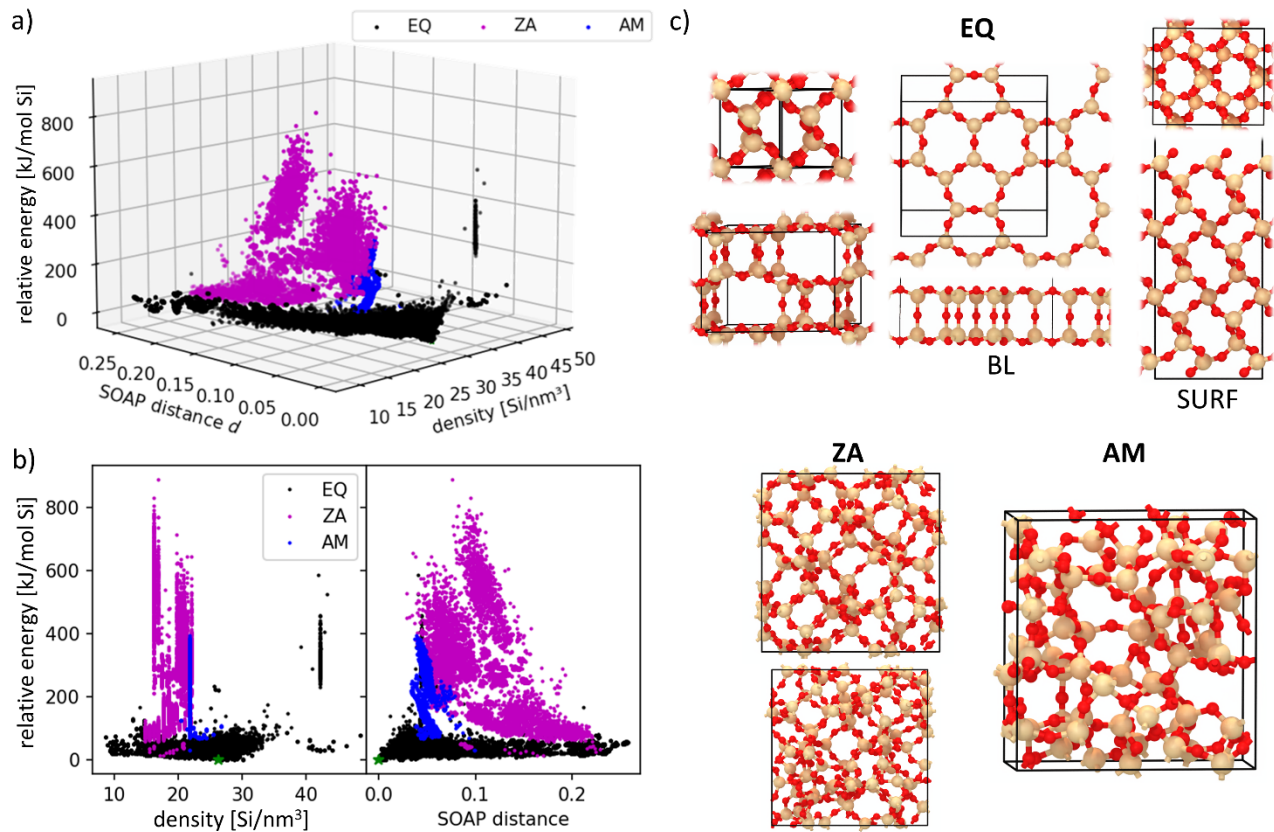


Figure S8: (a) Relative energies with respect to α -quartz (green star) of the final SCAN+D3 database as a function of atomic density and SOAP distance d (eq 1), (b) projections of (a), and (c) example structures close to equilibrium (EQ) including a silica bilayer (BL), and an α -quartz (001) surface model (SURF) showing dangling Si-O bonds (Fig. S8c). Most structures in EQ show tetrahedrally coordinated Si, except stishovite with six-fold coordinated Si. Structures with five-fold coordinated Si are part of AM corresponding to transition states in the liquid state. However, AM includes only densities close to silica glass density (2.2 g/cm^3 or 21.8 Si/nm^3). In contrast, ZA also contains high-energy structures and transition states (five-fold coordinated Si) at lower densities between $16\text{--}22 \text{ Si/nm}^3$ to interpolate the PES for simulations of the thermal collapse of zeolites. Most high-energy configurations show rather large SOAP distances from 0.05 to 0.2 , *i.e.*, low structural similarity compared to α -quartz. At lower SOAP distances are mainly higher density structures such as silica polymorphs with relative energies of less than 200 kJ/(mol Si) except for stishovite EQ configurations at densities larger than 40 Si/nm^3 (*cf.* Fig. S8b). Therefore, it is expected that the resulting NNPs inaccurately model reactive (high-energy) transformations of high-density silica phases which are beyond the scope of this work. Here, we focus on the accurate, reactive modeling of zeolites including low-density frameworks such as FAU (13.5 Si/nm^3) as described in Section 2.4.

Table S4 summarizes the test set errors of the NNP ensembles trained on the final DFT (PBE+D3 and SCAN+D3) datasets.

Table S4: Mean absolute (MAE) and root mean square error (RMSE) of the test sets.

NNPscan	Energy [meV/atom]		Forces [meV/Å]		NNPpbe	Energy [meV/atom]		Forces [meV/Å]	
	MAE	RMSE	MAE	RMSE		MAE	RMSE	MAE	RMSE
1	2.83	4.63	79.51	148.47	1	2.48	4.01	69.71	128.15
2	2.79	4.62	79.73	151.42	2	2.70	4.84	78.03	149.36
3	2.84	4.75	80.27	149.52	3	2.71	5.15	73.64	145.81
4	2.80	4.89	80.30	155.31	4	2.67	5.37	74.22	146.37
5	2.85	4.59	85.21	156.18	5	2.58	4.86	73.17	140.77
6	2.73	4.30	79.21	144.96	6	2.77	4.77	73.70	141.49

References

1. Wragg, D. S., Morris, R. E. & Burton, A. W. Pure Silica Zeolite-type Frameworks: A Structural Analysis. *Chem. Mater.* **20**, 1561–1570 (2008).
2. Armstrong, J. A. & Weller, M. T. Berylliosilicate Frameworks and Zeolites. *J. Am. Chem. Soc.* **132**, 15679–15686 (2010).
3. Mazur, M. *et al.* Synthesis of ‘unfeasible’ zeolites. *Nat. Chem.* **8**, 58–62 (2016).
4. Piccione, P. M. *et al.* Thermochemistry of Pure-Silica Zeolites. *J. Phys. Chem. B* **104**, 10001–10011 (2000).
5. Baerlocher, Ch. & McCusker, L. B. Database of Zeolite Structures: <http://www.iza-structure.org/databases/> (accessed: February 20, 2020).
6. Baerlocher, Ch., Meier, W. M. & Olson, D. M. *Atlas of Zeolite Framework Types*. (Elsevier, Amsterdam, 2001).
7. Bartók, A. P., Kondor, R. & Csányi, G. On representing chemical environments. *Phys. Rev. B* **87**, 184115 (2013).
8. De, S., Bartók, A. P., Csányi, G. & Ceriotti, M. Comparing molecules and solids across structural and alchemical space. *Phys. Chem. Chem. Phys.* **18**, 13754–13769 (2016).